International Symposium
On Turbulence and Shear Flow
Phenomena (TSFP-9)
June 30 - July 3, 2015 *Melbourne, Australia*

MECHANICAL ENERGY BUDGET OF TURBULENT RAYLEIGH-BÉNARD CONVECTION

Bishakhdatta Gayen
Research School of Earth Sciences
Australian National University
Acton, Canberra, ACT 0200
Bishakhdatta.Gayen@anu.edu.au

Graham O. Hughes
Research School of Earth Sciences
Australian National University
Acton, Canberra, ACT 0200
Graham.Hughes@anu.edu.au

Ross W. Griffiths
Research School of Earth Sciences
Australian National University
Acton, Canberra, ACT 0200
Ross.Griffiths@anu.edu.au

ABSTRACT

Turbulent Rayleigh-Bénard convection (RBC) is examined in terms of its mechanical energy budget. Three-dimensional large-eddy and direct numerical simulations are conducted at moderately large Rayleigh numbers. An expanded view of the mechanical energy pathways for RBC convection is developed for the the first time by recognising that mechanical energy includes gravitational potential energy and that the available component of this potential energy (APE) is the energy source for convection. The partitioning of energy pathways between large and small scales of motion is also analysed based on their corresponding temporal scales. The relative magnitudes of different pathways change significantly over the range of Rayleigh numbers $Ra \sim 10^7 - 10^{13}$. At $Ra < 10^7$ small-scale turbulent motions are energized directly from APE via turbulent buoyancy flux while kinetic energy is dissipated at comparable rates by both the large- and small-scale motions. In contrast, at $Ra \geq 10^{10}$ most of the APE goes into kinetic energy of the large-scale flow, and the large scales undergo shear instabilities that sustain small-scale turbulence. At large Ra one half of the total APE supply goes to viscous dissipation of kinetic energy and the other half to mixing of the thermal field. Therefore, mixing efficiency approaches 50% at large Ra, as also predicted by a scaling analysis. At large Rayleigh number the viscous dissipation is largely in the interior, while the irreversible mixing is largely confined to the unstable boundary layers. The inclusion of the mechanical energy in the budget provides new information on the roles of different length scales and on the mechanics of the interior and boundary layer.

Introduction

Rayleigh-Bénard convection (RBC) in a box is driven by buoyancy owing to heating from below and cooling from above. This is a idealized model for turbulent heat transfer, with many applications in astrophysics, atmospheric, environmental physics and human process technology. Its dynamics is governed by the Rayleigh number $Ra = g\alpha\Delta T H^3/(\nu\kappa)$ and the Prandtl number $Pr = \nu/\kappa$. Here, g is the gravitational acceleration, α is the thermal expansion coefficient, ΔT the temperature difference between the bottom and the top of the domain, H the height of the domain, and ν and κ are the kinematic viscosity and the thermal diffusivity, respectively. RBC has been studied extensively using theoretical, numerical and laboratory experiments with the aim of understanding the heat transport (measured commonly in the form of Nusselt number $Nu(Ra;Pr)$), the large scale circulation and the boundary layer properties including thermal structures and convective plume dynamics etc (Siggia, 1994; Ahlers *et al.*, 2009; Lohse & Xia, 2010), over a range of parameter regimes.

In RBC energy is injected in the form of available potential energy (which is a special from of potential energy essential for 'stirring' (Lorenz, 1955; Winters *et al.*, 1995; Peltier & Caulfield, 2003)) by steady thermal forcing at the top and bottom plates. Thermal boundary layers adjacent to plates soon trigger the flow motion at various scales by releasing available potential energy. Feedbacks of energy arises as the motions at different scales interact. Therefore, incorporating the potential energy reservoir in the mechanical energy frame work and allowing for energy transfer between its various forms are essential to understand more precisely both the boundary layer dynamics and the bulk of flow. This new and complete frame work (see Fig. 5 and Hughes *et al.* (2013), Gayen *et al.* (2013*b*)) for RBC includes all possible energy sources and sinks and also helps to quantify the complex turbulent mixing. Previous work has developed a different energy budget on RBC by considering only its kinetic and thermal forms (Deardorff & Willis, 1967; Siggia, 1994; Ahlers *et al.*, 2009; Lohse & Xia, 2010). The volume integrated dissipation of the total kinetic energy and the temperature field can be elegantly expressed in non-dimensional forms as $\varepsilon_u = \nu^3(Nu-1)RaPr^{-2}H^{-4}$ and $\varepsilon_\theta = \kappa\Delta T^2 NuRaH^{-2}$ (Siggia, 1994), respectively, under the Oberbeck-Boussinesq approximation. Unfortunately, the existing frame work is unable to provide much insight into the exchange of energy among its different forms, particularly where fluid motions

at different scales are involved. Our aim is to investigate the different forms of energy in the RBC and the pathways between them, in the addition to the potential energy budget and its decomposition into components of available and background potential energy.

Numerical methods

The computational domain consists of a rectangular box of height H, with bottom and top boundaries at z=$-0.5H, 0.5H$, and horizontal dimensions $L \times L$. The aspect ratio of the domain for most solutions is A=L/H=3, as we are most interested in wide layers, without side wall effects. Navier-Stokes (NS) equations under the Boussinesq approximation are written in Cartesian coordinates $[x, y, z]$ in non-dimensional form as:

$$\nabla \cdot \hat{\mathbf{u}} = 0, \tag{1}$$

$$\frac{D\hat{\mathbf{u}}}{D\hat{t}} = -\nabla \hat{p} + Pr\nabla^2 \hat{\mathbf{u}} + RaPr\hat{T}\mathbf{k} - \nabla \hat{\tau}, \tag{2}$$

$$\frac{D\hat{T}}{D\hat{t}} = \nabla^2 \hat{T} - \nabla \hat{\lambda}, \tag{3}$$

where the dimensionless quantities (denoted by a hat, after scaling mass, length, time and temperature by $\rho_0 H^3$, H, H^2/κ and $\Delta T = T_h - T_c$, respectively) are the velocity $\hat{\mathbf{u}} = (\hat{u}, \hat{v}, \hat{w})$, the temperature difference $\hat{T}$ from the reference value $\hat{T}_c$, the deviation $\hat{p}$ from the background hydrostatic pressure and the time $\hat{t}$. In the large eddy simulation (LES) $\hat{\mathbf{u}}$ and $\hat{T}$ are to be interpreted in the equations as filtered quantities (i.e. we drop the overbar conventionally used to denote filtering) and the quantities $\hat{\tau}$ and $\hat{\lambda}$ are the sub-gridscale (SGS) stress tensor and density flux vector, respectively. These require models for closure in LES. In direct numerical simulation (DNS) cases, $\hat{\tau}$ and $\hat{\lambda}$ are zero.

Present study coveres the Rayleigh number range $6 \times 10^6 \leq Ra \leq 6 \times 10^{12}$ with a fixed Prandtl number Pr=1. Direct numerical simulations (DNS) used a 512^3 grid, stretched in the z-direction, up to moderately large Rayleigh numbers $Ra \leq 6 \times 10^8$. Large eddy simulations (LES) were used for $6 \times 10^6 \leq Ra \leq 6 \times 10^{12}$ (with grids up to 1024^3). Additional DNS at Ra=6×10^8 were carried out for aspect ratios of A=1.5 and A=6.

The NS equations are numerically solved to obtain the velocity and the deviations from background density and pressure using a mixed spectral/finite difference algorithm on a staggered grid. Horizontal derivatives are treated with a pseudo-spectral method, and the vertical derivatives are computed with second-order finite differences. A third-order Runge-Kutta-Wray method is used for timestepping, and viscous terms are treated implicitly with the Crank-Nicolson method. A subgrid-scale model is used for the higher Ra number simulations. Detailed description of the subgrid-scale model and algorithm are found in Gayen *et al.* (2010). Periodicity is imposed in the horizontal, x and y, directions for velocity, pressure and density. Constant uniform temperatures T_H and T_C with non-slip velocity boundary conditions are applied at the bottom and top boundaries of the domain, respectively.

The grid resolution in the DNS was compared with the Kolmogorov scale, η, and the Batchelor scale η_b, where $\eta = \eta_b = (\nu^4/\varepsilon)^{1/3}$, based on the molecular viscosity ν and turbulent dissipation ε at $Pr = 1$. We adopt the criterion $l/\eta \leq \pi$ as proposed by Grötzbach (1983) and (Stevens *et al.*, 2010) (where l is the resolution in any given direction). The resolution satisfies the criterion in all three directions for DNS.

The resolution criterion ($l/\eta \leq \pi$) for DNS is not applicable to the coarser grid used for LES. The requirement for LES is that is captured faithfully the important part of the dissipation spectra as shown here. The dynamic diffusivity and viscosity adjust according to the slope of the cascade to ensure that dissipation is correct. Figure 1(a) compares dissipation spectra for velocity ($2\nu k^2 E_{u'}$) from the DNS and LES at the same Rayleigh number ($Ra = 6 \times 10^8$, the highest practical value for DNS). The two spectra overlap nicely up to the cut-off wavenumber for the LES. The unresolved part of the dissipation is modelled using a dynamic eddy viscosity to obtain accurate closure (Gayen *et al.*, 2010). We have chosen here the spectra in the thermal boundary layer at the level of maximum shear, and compare the results for a lower resolution LES (256^3) with a higher resolution DNS (512^3), as the most rigorous test. Similarly, the scalar dissipation spectra, $2\kappa k^2 E_{\Theta'}$ for temperature (figure 1b) shows good agreement up to to the cut-off wave number.

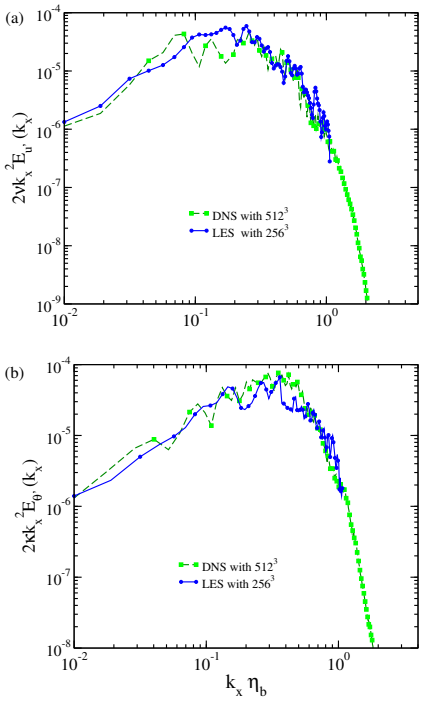

Figure 1. Dissipation spectra of (a) the horizontal velocity, u' and (b) the temperature fluctuations, Θ', at boundary layer, in the thermally equilibrated state.

Figure 2 shows the dissipation spectra for velocity at higher Ra numbers: $Ra = 6 \times 10^{10}$ and $Ra = 6 \times 10^{12}$, again in the boundary layer. Both techniques efficiently capture the dissipation up to a cut-off wave number. The grid resolution for LES cases maintained approximately $l \leq 10\eta$. The sub-gridscale model in the LES was based on a dynamic eddy viscosity and eddy diffusivity, as previously shown to be accurate for convection (Kimmel & Domaradzki, 2000; Peng *et al.*, 2006; Chung & Pullin, 2010; Shishkina & Wagner, 2008) (the detailed algorithms

are found in Armenio & Sarkar (2002); Gayen *et al.* (2010)).

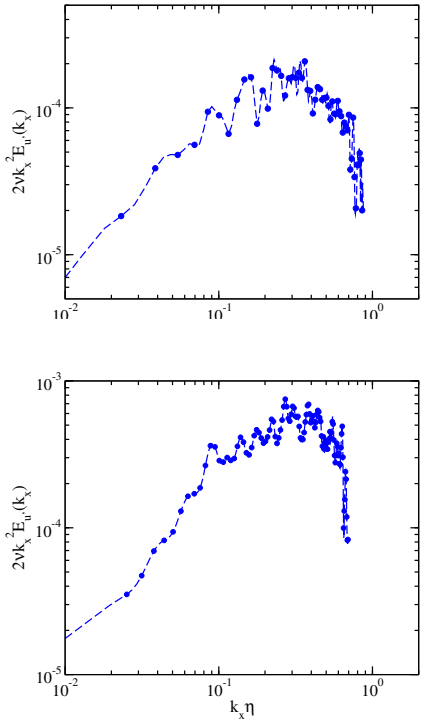

Figure 2. Dissipation spectra of the horizontal velocity, u' for LES run at (a) $Ra = 6\times10^{10}$ and (b) $Ra = 6\times10^{12}$, at boundary layer, in the thermally equilibrated state.

Results

Averaged profiles of temperature at its thermally equilibrated-state are shown for different Ra in figure 3. Simulations at $Ra > 10^{10}$ reveals the logarithmic temperature profile outside the viscous sub-layer, as reported by Ahlers *et al.* (2012). Fig. 4 presents the Nusselt number as a function of Rayleigh numbers, *Ra* for Pr= 1.0. The trend of *Nu* scaling agrees well with the previous experimental data of (Niemela *et al.*, 2000, 2001) and recent direct numerical simulation of Stevens *et al.* (2011) of RBC studied in cylindrical geometry of aspect ratio around $A \sim 0.25-0.5$. The present LES runs accurately capture heat transfer and reproduce the DNS results at $Ra \leq 6\times10^9$. The observed $Nu(Ra)$ scaling never exceeds the 1/3 power law, but a change of slope occurs around $Ra \sim 10^9$, consistent with previous DNS (Verzicco & Camussi, 2003) and experimental results (Niemela *et al.*, 2000, 2001). At the highest Ra considered here, there is no sign of a transition to the ultimate Kraichnan regime (Kraichnan, 1962; Lohse & Toschi, 2003).

Our main focus in this paper is to investigate the mechanical energy budget of the Rayleigh-Bénard convection based on the the generalised energetics framework as shown schematically in Fig. 5. This framework has been proposed

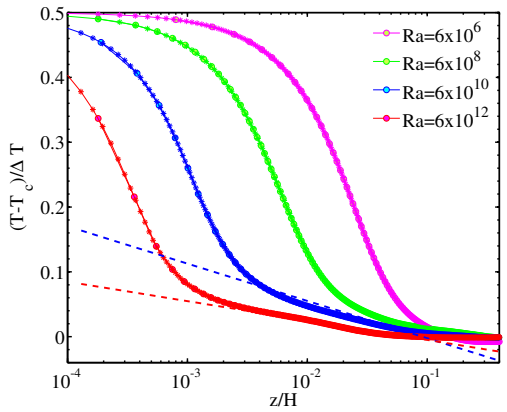

Figure 3. Horizontally averaged temperature profiles as a function of distance from the bottom and the top plate are shown. The dashed straight lines indicates the logarithmic part of the profiles.

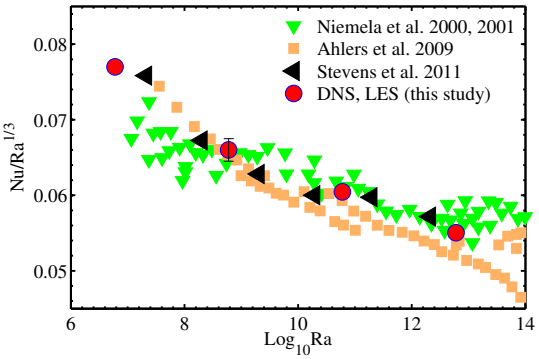

Figure 4. Values of $Nu/Ra^{1/3}$ obtained here (red) as a function of *Ra*, and comparison with previous works. Results at aspect ratios of $A = 1.5, 3, 6$ and $Ra = 6\times10^8$ all lie within the range of the bar shown at that *Ra*. The present DNS and LES at $Ra < 10^9$ are indistinguishable from each other.

by Hughes *et al.* (2009) for the global ocean circulation and recently investigated for horizontal convection Gayen *et al.* (2013*a*) and Griffiths *et al.* (2013), where convection is driven by placing both buoyancy sources at the same horizontal boundary. Detailed derivations of each terms in the frame work are found in Hughes *et al.* (2009, 2013). The forms of mechanical energy are kinetic energy $E_k = \rho_0/2\int u_i u_i \mathrm{dV}$ and potential energy $E_p = g\int z\rho \mathrm{dV}$, which are represented as two separated reservoirs with energy transfer between them via the buoyancy flux, $\Phi_z = g\int \rho w$ dV. Here, u_i is the velocity component in the ith direction and z is the vertical coordinate of the fluid parcel of volume dV. Transformation of mechanical energy that have a thermodynamic effect in the system are indicated notionally by a connection to the internal energy reservoir (see Tailleux (2009) for a more detailed description).

The potential energy, E_p, is further decomposed into components of background potential energy (BPE) $E_b = g\int z^* \rho dV$ and available potential energy, $E_a = E_p - E_b$ (Lorenz, 1955; Winters *et al.*, 1995). The background potatial energy of a fluid volume can be defined by assigning

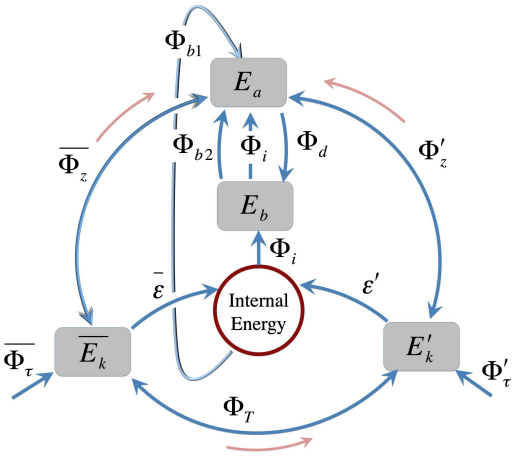

Figure 5. Schematic diagram showing the various forms and transformations of mechanical energy in a density-stratified flow of a linear Boussinesq fluid (Hughes *et al.*, 2009). Detailed descriptions are found in text. Where energy transfers can be bidirectional, an additional arrow denotes the positive direction.

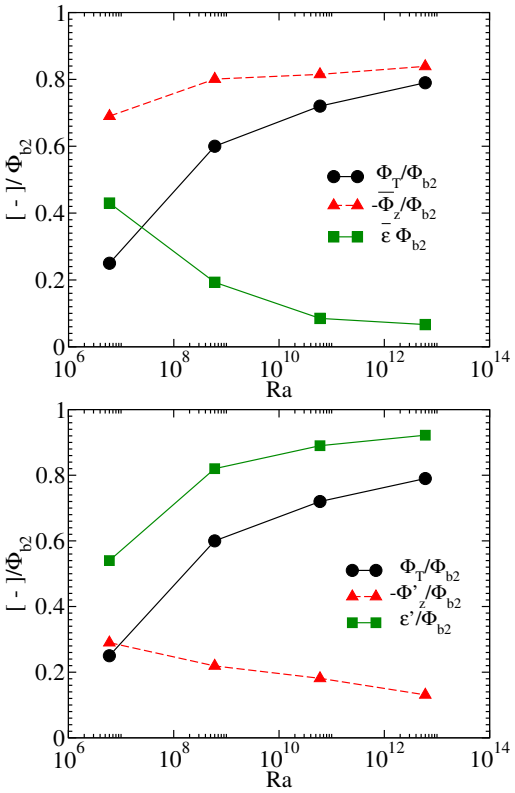

Figure 6. Time-averaged domain integrated values of normalized conversion rates for (a) mean and (b) fluctuation kinetic energy reservoirs at different *Ra* numbers. Here, normalization factor is the rate of APE supply from domain boundary $\Phi_{b2}(=\rho_0\kappa g\alpha\Delta T Nu L^2)$.

to each parcel a height $z* = z*(\rho)$ at which it would come to rest following a adiabatic relaxation of the density field. The role of available potential energy, which is the main driver of the fluid motion for the RBC, has been largely overlooked. APE and BPE exchange energy via irreversible mixing, $\Phi_d = -g\kappa\int(dz^*/d\rho)(\partial\rho/\partial x_i)^2 \mathrm{dV}$, the release of internal energy to potential energy by molecular diffusion (down the background gradient), $\Phi_i = -g\kappa L^2(\langle\rho\rangle_H - \langle\rho\rangle_0)$, and the differential buoyancy input at a given level, $\Phi_{b2} = g\kappa\oint z^*(\partial\rho/\partial x_i)n_i\ \mathrm{dS}$, where $\langle\rangle_z$ denotes a horizontal area average at height z and S is the surface bounding the volume. In physical terms Φ_{b2} represents the generation rate of available potential energy by maintaining a density field that is not in its adiabatically relaxed state and Φ_i corresponds to the rate at which the centre of mass of the volume would be raised or lowered by molecular diffusion if there was no convection. Viscous dissipation of kinetic energy occurs at the rate $\varepsilon = \rho_0\nu\int(\partial u_i/\partial x_j)^2$. The net buoyancy input at any level, $\Phi_{b1} = g\kappa\oint z^*(\partial\rho/\partial x_i)n_i$ gives the volume integrated rate of change of potential energy (and available potential energy) by net heating/cooling at each level.

We further decompose the kinetic energy reservoir into mean kinetic energy, $\overline{E}_k = \rho_0/2\int\overline{u}_i\overline{u}_i\mathrm{dV}$ and turbulent kinetic energy, $E'_k = \rho_0/2\int\overline{u'_iu'_i}\mathrm{dV}$. Here, mean (overbar) velocity and density components are obtained by time averaging over three turn-over time periods, $\tau_O\ (=\sqrt{H/g\alpha\Delta T})$. Fluctuating motions (primes) are evaluated after the deviation from the mean motion. Small scale turbulent motions in volume are sustained by extracting energy from the mean flow by shear production, $\Phi_T = -\rho_0\int\overline{u'_iu'_j}(\partial\overline{u}_i/\partial x_j)\mathrm{dV}$ and the turbulent buoyancy flux, $\Phi'_z = g\int\overline{\rho'w'}\mathrm{dV}$, which is supplied from available potential energy.

For RBC applied mechanical energy forcing in the form of surface stresses ($\overline{\Phi}_\tau$ and Φ'_τ) are absent and energy is supplied directly to the APE reservoir the rate $\Phi_{b2}\ (=\rho_0\kappa g\alpha\Delta T Nu L^2)$. We have normalized all the energy transfer rates by the Φ_{b2} to compare various cases in Fig. 6. Our numerical simulation results for RBC confirm that the rate of dissipation due to irreversible mixing exactly is equal to the generation rate of APE; $\Phi_d = \Phi_{b2}$, which has been theoretically predicted by Hughes *et al.* (2009) and recently shown for horizontal convection by Gayen *et al.* (2013*a*). For RBC Φ_i is negative and negligible compared to other conversion terms. At low *Ra* number energy is transferred to both the mean and the fluctuating kinetic motions via buoyancy flux at comparable rates. Generation of small scale motions by shear production is small. In physical terms, small scale convection is the primary source of turbulent motions. Viscous dissipation occurs at approximately equal rate from both the mean motions, $\overline{\varepsilon}$, and the small scale motions, ε'. With increasing *Ra* number a large scale circulation, known as "wind", develops (Niemela *et al.*, 2001) inside the box, and corresponds to a significant change in the energy pathways in Fig. 5. More energy is pumped to the kinetic energy reservoir through mean buoyancy flux, because small scale convective plumes are swept into a large scale flow (Shang *et al.*, 2003; Ahlers *et al.*, 2009). Viscous dissipation directly from large scale structures is not efficient and decreases with *Ra* number. At higher *Ra* the wind velocity of the large scale circulation increases and the velocity boundary layer thickness decreases significantly, resulting in enhancement of the boundary shear (Grossmann & Lohse, 2002; Ahlers *et al.*, 2009). Small scale motions are initiated through shear production from large scale mean flow. At $Ra \sim 10^{13}$ almost 80% of the turbulence is produced by shear compared to a 20% contribution the from the APE via turbulence buoyancy flux due to small scale convective

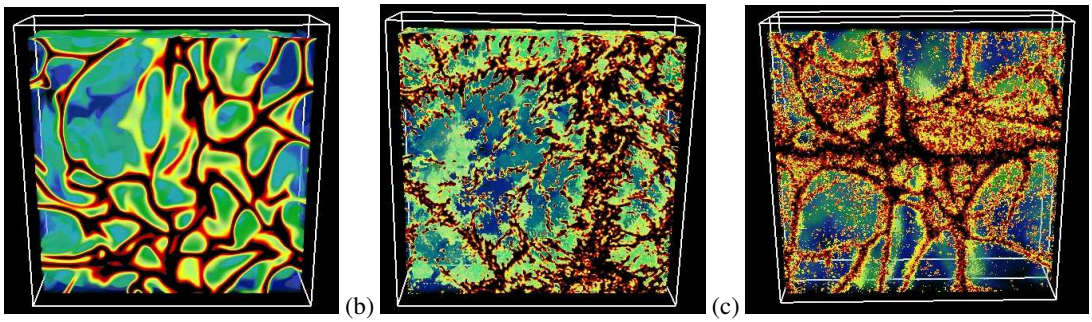

Figure 7. Visualization of the thermal structures by the iso-surfaces of normalized temperature field, $(T-T_C)/\Delta T$ inside a a sub-domain which extends vertically from z=0.3δ_{95} to $z = H/2$ from the bottom plate at (a) $Ra = 6\times10^6$, (b) $Ra = 6\times10^8$ and (c) $Ra = 6\times10^{12}$. Here dark color indicates the lightest buoyant fluid.

plumes. These small scale motions are dissipated viscously ε'. Therefore, RBC at higher *Ra* numbers is the results of primary energy flow from APE to mean KE, then mean KE to TKE via shear, whereas it is dissipated by viscosity. This corresponds to a large energy transfer through left handed pathways of the energy wheel in Fig. 5.

Enhancement of the boundary layer shear owing to large scale circulation at higher Rayleigh number is also evident from the flow structures in the proximity of the top/bottom plates, as portrayed by iso-surfaces of thermal field in Fig. 7. At small Rayleigh number ($Ra \sim 10^7$) cell structures are coherent and bounded by convergence lines that corresponds to the base of sheet plumes of rising buoyant fluid (Puthenveettil & Arakeri, 2005; Zhou *et al.*, 2007). Alignment of the convergence lines is random and unaffected by the weak circulation ('wind') at the box scale. Mushroom like structures form at the nodal points where sheet plumes collide and convolute as previously investigated by Zhou *et al.* (2007) in laboratory experiment of RBC using water as a working fluid at $Ra \sim 5\times10^8 - 6\times10^9$. The thermal structures change significantly at higher Rayleigh numbers under the influence of the large scale 'wind'. Sheet plumes are instead aligned along the direction of wind shear and merge together along a line to form a mega plume. A tendency to form mega plumes is evident at $Ra \sim 10^9$, but these the large scale structures along with well organized convergence lines are very clear at $Ra \sim 10^{13}$, as shown in Fig. 7(c). Similar observations have been made experimentally by Puthenveettil & Arakeri (2005) at $Ra \sim 10^{11}$. At large *Ra* numbers, a homogeneous distribution of small convectiive plumes inside the boundary layer is absent, reflecting weak energy transfer from APE to fluctuating kinetic energy reservoir via turbulent buoyancy flux, Φ_z' (ref. Fig. 6).

Rayleigh-Bénard convection can be characterized as an efficient mechanism of heat transport in a stratified flow in terms of the proportion of supplied energy that results in mixing, i.e. the mixing efficiency (Hughes *et al.*, 2009; Peltier & Caulfield, 2003; Gayen *et al.*, 2013*a*) defined as $\eta = (\Phi_d - \Phi_i)/(\Phi_d - \Phi_i + \varepsilon)$. This evaluates to $\eta \approx 0.5001$ from our numerical simulation for the highest *Ra* considered here, which in agreement with resent theoretical estimations, $(\eta \to 1/2)$ for RBC at higher Ra regime (Hughes *et al.*, 2013; Gayen *et al.*, 2013*b*).

Conclusion

RBC has been studied in the three-dimensional rectangular box geometry using direct and large eddy simulation. The constant thermal forcing which is source of system available potential energy to maintain the flow. The supply of energy to support turbulent motions occurs in a manner that depends strongly on Rayleigh number. At low Ra both the small and the large scale motions extract a comparable amount of APE via the buoyancy flux, and there is small exchange of energy between the mean and the turbulent kinetic energy reservoirs. At higher Ra a significant portion of the APE supply (80% for highest Ra) goes to mean motions that further generate small scale turbulent motion via shear production throughout the domain, particularly large in magnitude inside the boundary layer. Shear across the boundary layer is seen to set the large thermal structure by forcing sheet plumes to converge. The irreversible mixing that is required to balance the boundary buoyancy forcing (APE generation) is concentrated mostly inside the thermal boundary layer.

REFERENCES

Ahlers, G., Bodenschatz, E., Funfschilling, D., Grossmann, S., He, X., Lohse, D., Stevens, R. J. A. M. & Verzicco, R. 2012 Logarithmic temperature profiles in turbulent rayleigh-bénard convection. *Phys. Rev. Lett.* **109**, 114501.

Ahlers, G., Grossmann, S. & Lohse, D. 2009 Heat transfer and large scale dynamics in turbulent rayleigh-bénard convection. *Rev. Mod. Phys.* **81**, 503–537.

Armenio, V. & Sarkar, S. 2002 An investigation of stably stratified turbulent channel flow using large-eddy simulation. *Journal of Fluid Mechanics* **459**, 1–42.

Chung, D. & Pullin, D. I. 2010 Direct numerical simulation and large-eddy simulation of stationary buoyancy-driven turbulence. *Journal of Fluid Mechanics* **643**, 279–308.

Deardorff, J. W. & Willis, G. E. 1967 Investigation of turbulent thermal convection between horizontal plates. *Journal of Fluid Mechanics* **28**, 675–704.

Gayen, Bishakhdatta, Griffiths, Ross W., Hughes, Graham O. & Saenz, Juan A. 2013*a* Energetics of horizontal convection. *Journal of Fluid Mechanics* **716**.

Gayen, B., Hughes, G. O. & Griffiths, R. W. 2013*b* Completing the mechanical energy pathways in turbulent rayleigh-bénard convection. *Phys. Rev. Lett.* **111**, 124301.

Gayen, B., Sarkar, S. & Taylor, J. R. 2010 Large eddy sim-

ulation of a stratified boundary layer under an oscillatory current. *Journal of Fluid Mechanics* **643**, 233–266.

Griffiths, Ross W., Hughes, Graham O. & Gayen, Bishakhdatta 2013 Horizontal convection dynamics: insights from transient adjustment. *Journal of Fluid Mechanics* **726**, 559–595.

Grossmann, S. & Lohse, D. 2002 Prandtl and rayleigh number dependence of the reynolds number in turbulent thermal convection. *Phys. Rev. E* **66**, 016305.

Grötzbach, G. 1983 Spatial resolution requirements for direct numerical simulation of the rayleigh-bnard convection. *Journal of Computational Physics* **49** (2), 241 – 264.

Hughes, G.O., Hogg, A.McC & Griffiths, R.W. 2009 Available potential energy and irreversible mixing in the meridional overturning circulation. *J. Phys. Oceanogr.* **39**, 3130–3146.

Hughes, Graham O., Gayen, Bishakhdatta & Griffiths, Ross W. 2013 Available potential energy in rayleighbnard convection. *Journal of Fluid Mechanics* **729**.

Kimmel, Shari J. & Domaradzki, J. Andrzej 2000 Large eddy simulations of rayleighbnard convection using subgrid scale estimation model. *Physics of Fluids (1994-present)* **12** (1), 169–184.

Kraichnan, R. H. 1962 Turbulent thermal convection at arbitrary prandtl number. *Physics of Fluids (1958-1988)* **5** (11), 1374–1389.

Lohse, D. & Toschi, F. 2003 Ultimate state of thermal convection. *Phys. Rev. Lett.* **90**, 034502.

Lohse, D. & Xia, K.-Q. 2010 Small-scale properties of turbulent rayleigh-bnard convection. *Annual Review of Fluid Mechanics* **42** (1), 335–364.

Lorenz, E. 1955 Available potential energy and the maintenance of the general circulation. *Tellus A* **7** (2).

Niemela, J. J., Skrbek, L., Sreeenivasan, K. R. & Donnelly, R. J. 2000 Turbulent convection at very high rayleigh numbers. *Nature* **404**, 837–840.

Niemela, J. J., Skrbek, L., Sreeenivasan, K. R. & Donnelly, R. J. 2001 The wind in confined thermal convection. *Journal of Fluid Mechanics* **449**, 169–178.

Peltier, W. R. & Caulfield, C. P. 2003 Mixing efficiency in stratified shear flows. *Annual Review of Fluid Mechanics* **35** (1), 135–167.

Peng, S.-H., Hanjalic, K. & Davidson, L. 2006 Large-eddy simulation and deduced scaling analysis of rayleighbnard convection up to ra = 109. *Journal of Turbulence* **7**, N66.

Puthenveettil, B. A. & Arakeri, J. H. 2005 Plume structure in high-rayleigh-number convection. *Journal of Fluid Mechanics* **542**, 217–249.

Shang, X.-D., Qiu, X.-L., Tong, P. & Xia, K.-Q. 2003 Measured local heat transport in turbulent rayleigh-bénard convection. *Phys. Rev. Lett.* **90**, 074501.

Shishkina, O. & Wagner, C. 2008 Analysis of sheet-like thermal plumes in turbulent rayleighbnard convection. *Journal of Fluid Mechanics* **599**, 383–404.

Siggia, E D 1994 High rayleigh number convection. *Annual Review of Fluid Mechanics* **26** (1), 137–168.

Stevens, R. J. A. M., Lohse, D. & Verzicco, R. 2011 Prandtl and rayleigh number dependence of heat transport in high rayleigh number thermal convection. *Journal of Fluid Mechanics* **688**, 31–43.

Stevens, R. J. A. M., Verzicco, R. & Lohse, D. 2010 Radial boundary layer structure and nusselt number in rayleighbnard convection. *Journal of Fluid Mechanics* **643**, 495–507.

Tailleux, R. 2009 On the energetics of stratified turbulent mixing, irreversible thermodynamics, boussinesq models and the ocean heat engine controversy. *Journal of Fluid Mechanics* **638**, 339–382.

Verzicco, R. & Camussi, R. 2003 Numerical experiments on strongly turbulent thermal convection in a slender cylindrical cell. *Journal of Fluid Mechanics* **477**, 19–49.

Winters, K. B., Lombard, P. N., Riley, J. J. & D'Asaro, E. A. 1995 Available potential energy and mixing in density-stratified fluids. *Journal of Fluid Mechanics* **289**, 115–128.

Zhou, Q., Sun, C. & Xia, K.-Q. 2007 Morphological evolution of thermal plumes in turbulent rayleigh-bénard convection. *Phys. Rev. Lett.* **98**, 074501.